Materials Horizons

ROYAL SOCIETY OF CHEMISTRY

COMMUNICATION

View Article Online
View Journal | View Issue

Cite this: *Mater. Horiz.*, 2023, **10**, 5214

Received 31st July 2023,
Accepted 8th September 2023

DOI: 10.1039/d3mh01201h

rsc.li/materials-horizons

Dilute Gd hydroxycarbonate particles for localized spin qubit integration†

Inés Tejedor, [a] Ainhoa Urtizberea, [b] Eva Natividad, [b] Jesús I. Martínez, [a] Ignacio Gascón [a] and Olivier Roubeau *[a]

Molecular spins are considered as the quantum hardware to build hybrid quantum processors in which coupling to superconducting devices would provide the means to implement the necessary coherent manipulations. As an alternative to large magnetically-dilute crystals or concentrated nano-scale deposits of paramagnetic molecules that have been studied so far, the use of pre-formed sub-micronic spherical particles of a doped Gd@Y hydroxycarbonate is evaluated here. Particles with an adjustable number of spin carriers are prepared through the control of both particle size and doping. Bulk magnetic properties and continuous wave and time-domain-EPR spectroscopy show that the Gd spins in these particles are potential qubits with robust quantum coherence. Monolayers of densely-packed particles are then formed interfacially and transferred successfully to the surface of Nb superconducting resonators. Alternatively, these particles are disposed at controlled localizations as isolated groups of a few particles through Dip-Pen Nanolithography using colloidal organic dispersions as ink. Altogether, this study offers new material and methodologies relevant to the development of viable hybrid quantum processors.

New concepts

We report alternative material types and methodologies to integrate controlled numbers of spin qubits on superconducting devices. These are aimed at engineering a hybrid quantum computing architecture, for which macroscopic magnetically-dilute crystals and nanoscopic concentrated deposits of paramagnetic molecules have so far been coupled to superconducting resonators. These strategies, however do not allow at the same time to maintain coherence properties, control qubit orientation and localization and adjust the number of spins to the improving sensitivity/quality of state-of-the-art resonators. To fulfill these requirements, this work uses pre-formed sub-micronic particles of yttrium hydroxycarbonate doped with Gd(III) ions. The use of the isotropic Gd(III) ion in a diamagnetic host with few nuclear spins gives access to robust qubits with reasonable coherence times. Control of the particle size and doping allows adjustment of the number of qubits per particle to the adequate range, while the ability to disperse the particles without damage permits the use of Langmuir–Blodgett and Dip-Pen Nanolithography techniques to respectively transfer monolayers of particles or locate a few isolated particles on the surface of Nb superconducting structures.

Introduction

Current technological development of quantum computers focuses on superconducting hardware, with increasing numbers of quantum bits and impressive, though debated, achievements.[1] Yet, the current low overall fidelity of these,[2] and the remaining necessity to scale to much larger numbers of qubits to implement sufficiently effective error-correction codes[3] makes other physical embodiments of the quantum hardware still very relevant.[4] Among spin-based qubits, the electronic spin carried by paramagnetic molecules, either organic radicals or transition metal ion complexes, has arisen as a real alternative.[5] This is due to the demonstration that sufficiently long quantum coherence times can be reached,[6] together with specific advantages of these molecular qubits, in particular making moles of perfectly identical qubits in one sole reaction, the ability to manipulate isolated qubits through solution-based methods, and the possibility of designing molecules that could operate as a quantum gate at the single-molecule level (either through multiple qubits weakly interacting or through coupling with nuclear spins).[5,7] Some of these potentials have been evaluated theoretically[8] or even demonstrated experimentally,[9] but the necessity to eventually read/manipulate these molecular qubits/qugates individually and in large numbers requires their wiring-up within a macroscopic

[a] *Instituto de Nanociencia y Materiales de Aragón (INMA), CSIC and Universidad de Zaragoza, Plaza San Francisco s/n, 50009 Zaragoza, Spain*
[b] *Instituto de Nanociencia y Materiales de Aragón (INMA), CSIC and Universidad de Zaragoza, Campus Río Ebro, María de Luna 3, 50018 Zaragoza, Spain. E-mail: roubeau@unizar.es*

† Electronic supplementary information (ESI) available: IR spectra, PXRD, TGA and EPR data, SEM images and analysis, and XPS survey spectra. See DOI: https://doi.org/10.1039/d3mh01201h

device. For this, a hybrid quantum architecture is being developed in which the molecular qubits are to be integrated at the surface of superconducting circuits.[10] So far, experiments have been done on large spin ensembles in macroscopic crystals allowing broad-band spectroscopy as well as pulsed experiments to be performed.[11] Going towards single-spin use, as done through STM techniques for individual atoms on surfaces or electrical readout/driving of Tb phthalocyanines integrated into transistor-like configurations,[12] relies on the improvement of the sensitivity of the superconducting resonators. It will also require techniques that allow disposing the spin carrier with a controlled and homogeneous orientation at specific localizations of the superconducting architecture, *i.e.* nanoconstrictions made to increase the local magnetic field by various orders of magnitude.[13] Recently, nanodroplets of the organic radical DPPH were deposited using Dip-Pen Nanolithography (DPN),[14] showing that strong coupling of the molecular qubits to the photon(s) in the superconducting circuit is attainable.[15] Another strategy could be qubit monolayers formed under UHV,[16] but this is limited to systems amenable to sublimation, requires very clean and flat surfaces and does not allow control of localization, while the interaction with the superconducting active surface can alter the electronic properties of the deposited molecules.[17] We have reported an alternative strategy through which diluted nanodomains of 2D planes built from metalloporphyrin qubit nodes can be transferred onto or directly formed *in situ* at the surface of superconducting lines.[18] This allows disposing qubits with homogeneous and controlled orientation, thanks to the underlying periodicity of the formed material. The number of spins can also be adjusted by dilution to match the sensitivity of current state-of-the-art resonators, albeit without allowing a nanoscale localization control. It is thus relevant to have the means to dispose with nanoscopic control ensembles with an adjustable number of spins. For this purpose we focus here on pre-formed submicronic Y(OH)(CO_3) particles doped with varying amounts of Gd (Scheme 1). The use of a highly isotropic spin carrier such as Gd(III) makes the necessary control of qubit orientation less stringent, while Gd(III) ions in molecular complexes have been shown to be valid qubit/qudit embodiments.[19] The use of doped particles also ensures avoiding too strong direct qubit–surface interaction. We first show that the obtained particles exhibit reasonable quantum coherence and then determine the conditions to either transfer them to solid substrates as compact monolayers or dispose them on superconducting resonators as a few isolated particles.

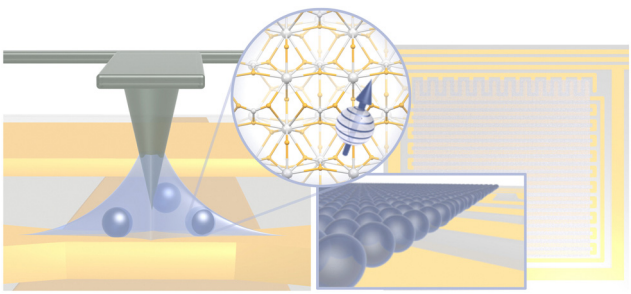

Scheme 1 Schematic views of the targeted disposition of pre-formed Gd@Y hydroxycarbonate particles onto superconducting devices: a few isolated particles on nanoconstrictions through DPN (left), or compact monolayers covering the sensing area of superconducting lumped element resonators (right).

Results and discussion

Synthesis of particles with adjustable size and composition

Lanthanide hydroxycarbonate particles were originally studied as precursors of the corresponding oxides.[20] The synthesis uses the thermal decomposition of urea as a controlled source of carbonate, resulting in the formation of particles with good size homogeneity, the size being adjustable synthetically in the range of 0.1–0.6 μm. The pure Y[20b,c] and Gd[20a] as well as doped Ce@Y systems[20c] have been studied. Here, we have adapted the reported conditions, to obtain Gd@Y particles with targeted Gd contents of 0.1, 1.0 and 10% and targeted diameters of either 100 or 300 nm, in the size range of the nanoconstrictions made so far in Nb superconducting devices (see ESI† for details).[13,15] As previously reported for other compositions, the obtained particles are amorphous (Fig. S1, ESI†), but IR spectroscopy shows the carbonate C–O bands ν_3 at 1502 and 1377 cm^{-1}, ν_1 at 1088 cm^{-1} and ν_2 at 839 cm^{-1}, altogether characteristic of coordinated carbonate ions,[21] and indeed similar to crystalline M(OH)(CO_3) materials.[22] A shoulder at *ca.* 1645 cm^{-1} likely corresponds to the deformation band of hydration water, while O–H stretching vibrations of both water and hydroxyl groups appear in the form of a broad band covering the 3000–3500 cm^{-1} range (Fig. S2, ESI†). Thermogravimetric analysis indicates the presence of minor amounts of water (Fig. S3, ESI†), so that the $Gd_xY_{1-x}OHCO_3$ formula will be used throughout. The Gd/Y ratio was determined by ICP-AES for the larger particles, giving compositions of $Gd_{0.003}Y_{0.997}OHCO_3$, $Gd_{0.006}Y_{0.994}OHCO_3$ and $Gd_{0.086}Y_{0.914}OHCO_3$, respectively. SEM observations show that relatively monodisperse spherical particles are obtained. Analysis of the particle size as derived from SEM images (Fig. 1 and Fig. S4, S5, ESI†) indicates a good size homogeneity in all cases, with diameters of 329(24)/287(23)/354(40) and 212(23)/206(22)/187(19) nm respectively for the targeted large and small particles, which is also confirmed by DLS on dilute dispersions (see below). Such good size homogeneity is important to ensure that the number of spins does not vary significantly from particle to particle. The control of the level of doping is relatively good, since the obtained compositions do not depart significantly from the targeted ones (Fig. S6 and Table S1, ESI†), but we have found batch-to-batch variations of up to 50% in terms of average size.

Magnetic properties

Bulk isothermal magnetization at increasing fields was determined for all $Gd_xY_{1-x}OHCO_3$ particles, and compared with those of the pure Gd analogue (Fig. 2(a) and Fig. S6, ESI†), which we study for its high magnetocaloric effect.[23] While the

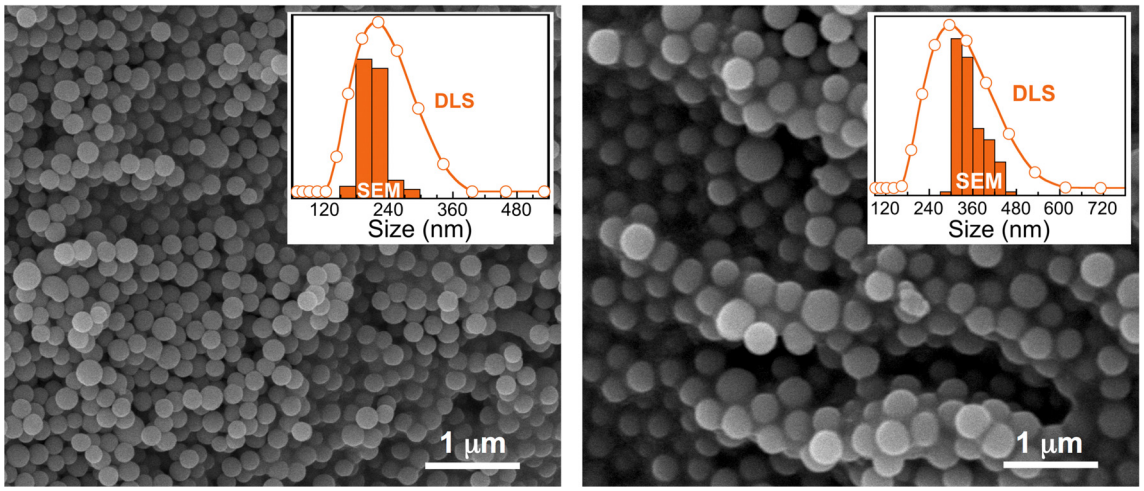

Fig. 1 SEM images of small (left) and large (right) $Gd_{0.086}Y_{0.914}OHCO_3$ particles. Insets: SEM size distribution histogram (bars) and DLS hydrodynamic size distribution (empty circles with line) measured on MeOH dispersions.

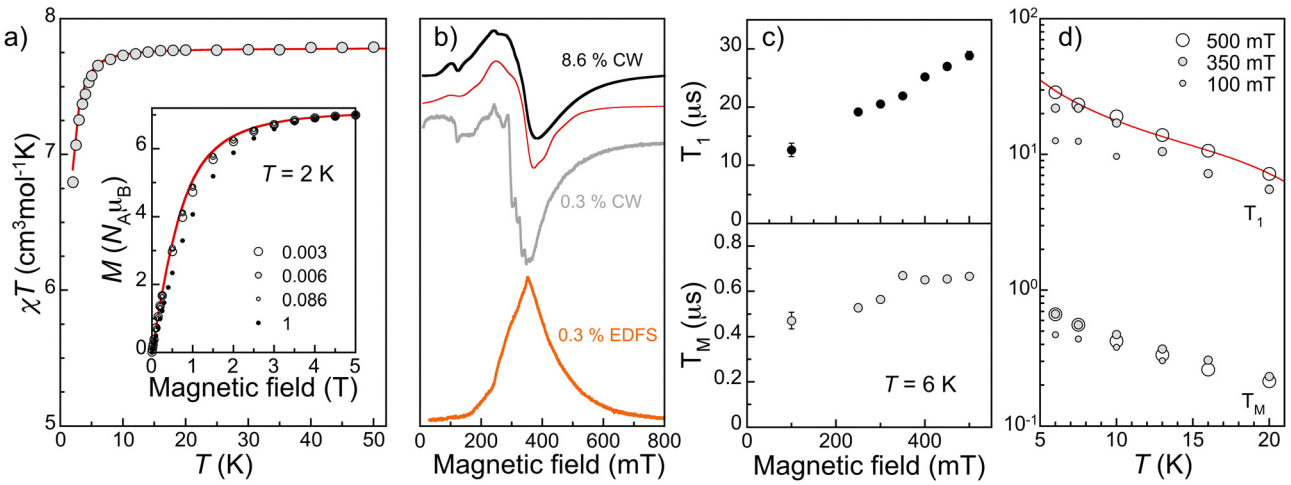

Fig. 2 (a) χT *vs.* T plot (χ is the molar magnetic susceptibility) for $Gd_{0.006}Y_{0.994}OHCO_3$ large particles. The solid red line corresponds to the curve calculated with the curry function of Easyspin[24] with the same parameters as those used to simulate the cw-EPR spectrum (see text). Inset: Magnetization isotherms at 2 K for $Gd_xY_{1-x}OHCO_3$ large particles with indicated x values. The red line is the Brillouin function for S = 7/2 and g = 2.02. All data are scaled to pure $GdOHCO_3$. (b) X-band cw-EPR spectrum of $Gd_{0.086}Y_{0.914}OHCO_3$ particles at RT (black line) and its simulation (red trace) considering a S = 7/2 spin with g = 2.10, D = 1.12 GHz and E = 0, together with the cw (RT, grey line) and EDFS (6 K, orange line) spectra of $Gd_{0.003}Y_{0.997}OHCO_3$ particles. (c) Field and (d) temperature dependences of the mean longitudinal relaxation time T_1 and phase memory time T_M for $Gd_{0.003}Y_{0.997}OHCO_3$ particles. The red line is the simulation of the T_1 *vs.* T data at 500 mT to a model contemplating direct and Raman processes (see text).

latter deviates from the Brillouin function of an S = 7/2 spin at intermediate fields due to the effect of antiferromagnetic interactions, the M *vs.* H data for the three dilutions studied here are very close to it, indicating a strong reduction of these interactions, already in the more concentrated $Gd_{0.086}Y_{0.914}$-$OHCO_3$ particles. The decrease of the product χT observed at low temperatures (Fig. 2(a), χ is the molar magnetic susceptibility) is in this respect likely due to the effect of the small but measurable Gd(III) ion magnetic anisotropy (see below). Eventually, the Gd/Y ratio derived indirectly through the scaling of the raw M *vs.* H data is in excellent agreement with that from ICP-AES (Fig. S6 and Table S1, ESI†).

Continuous-wave electron paramagnetic resonance (cw-EPR) spectra of the $Gd_{0.086}Y_{0.914}OHCO_3$ and $Gd_{0.003}Y_{0.997}OHCO_3$ larger particles were acquired at the X-band, only differing in the arising of some sharper lines in the more magnetically dilute sample (Fig. 2(b)). A reasonably good simulation of the spectra is obtained with Easyspin[24] setting D = 1.12 GHz, $|E| <$ 0.06 GHz and g = 2.10. These parameters also provide a good simulation of the temperature dependence of the magnetic susceptibility (Fig. 2(a)), confirming the absence of any significant magnetic interactions. The very small orthorhombicity $|E|/D$ could be due to the high local symmetry of the Gd site in crystalline $GdOHCO_3$,[22a] maintained despite the amorphous

nature of our particles. The zero-field splitting D term is actually very similar to that derived for the polyoxometallate $Gd_{0.01}Y_{0.99}W_{30}$ prototype 3-qubit,[25] which means that the low-energy magnetic level schemes will not differ significantly, thus providing the conditions for a potential 3-qubit.[19b]

Spin dynamics and quantum coherence

Pulsed-EPR was then used to confirm and evaluate the presence of quantum coherence in the $Gd_{0.003}Y_{0.997}OHCO_3$ large particles. The Echo-Detected Field-Swept (EDFS) spectrum at 6 K is in good agreement with the cw-EPR spectrum, although the sharp lines are not resolved (Fig. 2(b)). In any case, this confirms that the echo detected over the whole range of the cw-EPR spectrum corresponds to the isolated Gd(III) ions. The phase memory T_M and spin lattice relaxation T_1 times were determined at various fields from 100 to 500 mT and in the temperature range of 6–20 K (Fig. S8, S9 and Table S2, ESI†). At 6 K, both T_M and T_1 increase with the applied magnetic field, respectively from 12.6 to 28.9 and 0.47 to 0.67 μs from 100 to 500 mT (Fig. 2(c)). Interestingly, T_1 is relatively long for a Gd(III) species, for example about 1 order of magnitude longer than in $Gd_{0.01}Y_{0.99}W_{30}$ (2.3–2.8 μs at 6 K),[19b] possibly the result of a more rigid lattice with respect to molecular materials.[26] The observed T_1 in $Gd_{0.003}Y_{0.997}OHCO_3$ remains reasonably short, *i.e.* would not impede fast initialization of the qubit, but increasing T_1 is relevant because it has been observed to be limiting T_M in Ln-based qubits.[27] Indeed, the T_M values are also longer than in $Gd_{0.01}Y_{0.99}W_{30}$, but only by about 10%.[19b] The effect on decoherence of a reduced interaction with the nuclear spin bath due to the presence of only one proton in $Gd_xY_{1-x}OHCO_3$ is expected to be only relevant at the ms timescale.[28] Thus, the observed increase of T_M in the μs range would rather be associated with a more dilute nature, resulting in a reduction of decoherence through pair-flip with remaining Gd(III) sites. The lower concentration used here with respect to $Gd_{0.01}Y_{0.99}W_{30}$ is however in part compensated by a higher density, which likely explains the limited increase in T_M. Upon increasing the temperature, T_1 decreases, down to 5.55 μs at 20 K and 350 mT, a behavior paralleled in T_M, which decreases down to 0.23 μs (Fig. 2(d)). This probably indicates that T_M remains in part T_1-limited, confirming the importance of improving T_1. The temperature dependence of T_1 can be reasonably simulated with direct and Raman relaxation processes using the expression $T_1^{-1} = aT + bT^9$ with $a = 0.0056(2)$ K s^{-1} and $b = 5(3)\cdot10^{-14}$ s^{-1} K^{-9}.[29] Altogether, our magnetically dilute $Gd_xY_{1-x}OHCO_3$ particles are carriers of valid spin qubits, with a number of qubits per particle that can be tuned through both the level of magnetic dilution and the diameter of the spherical particles down to tens of thousands. Experimentally feasible further dilution would

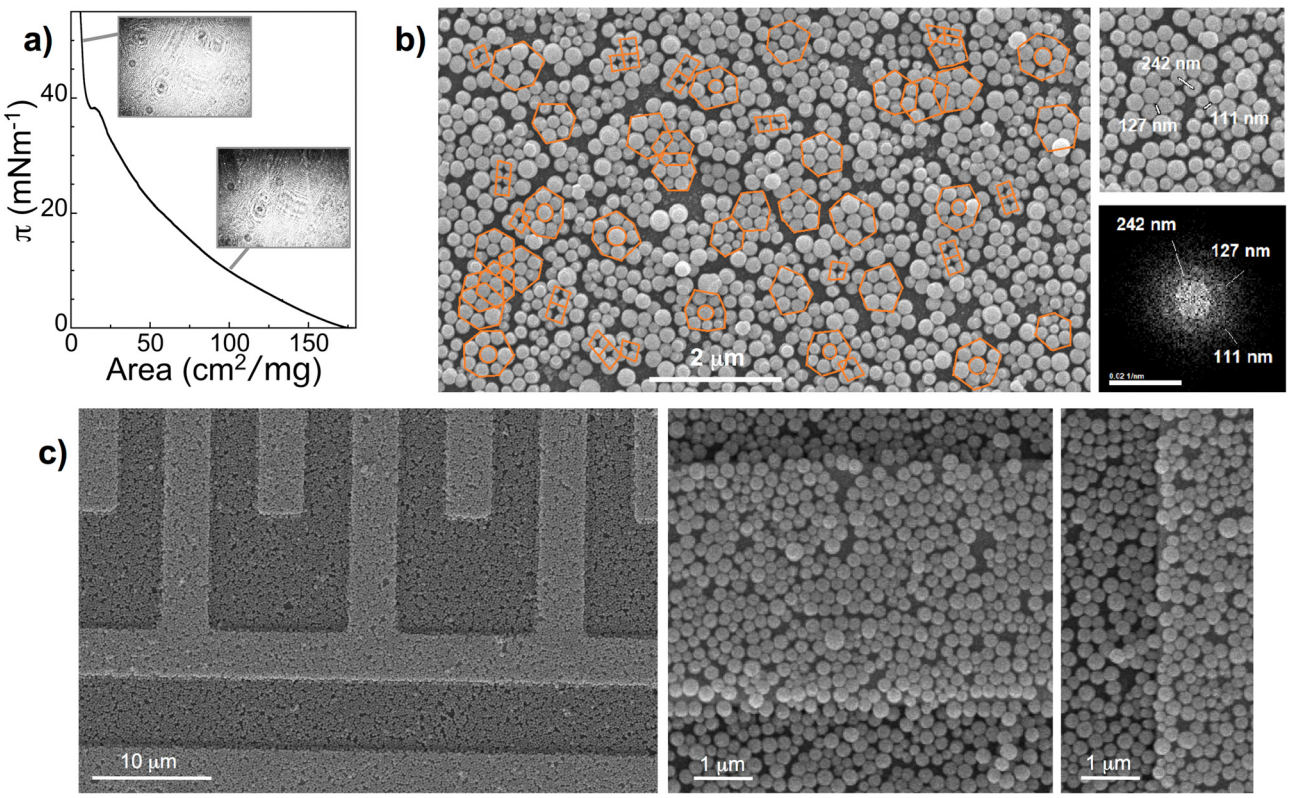

Fig. 3 (a) Representative surface pressure–area (π–A) isotherm obtained for the $Gd_{0.003}Y_{0.997}OHCO_3$ particles. (b) SEM image of an LB film obtained upon vertical transfer onto a Si wafer at 55 mN m^{-1} showing domains (highlighted in orange) with local hexagonal, imperfect hexagonal and square particle arrangements. A small area together with its FFT analysis is shown on the right. The features observed in the FFT are ascribed to hexagonal arrangements. (c) SEM images of a deposit made through LB transfer at 55 mN m^{-1} on a chip with superconducting Nb lumped element resonators.

allow the range of hundreds to thousands of qubits per particle to be reached.

Integration through Langmuir–Blodgett transfer

As a first means to dispose our $Gd_xY_{1-x}OHCO_3$ particles on the surface of devices, the possibility to use Langmuir–Blodgett methods was investigated. For this, the ability to form sufficiently stable and concentrated dispersions in volatile organic solvents such as $CHCl_3$ or CH_2Cl_2 is key. Optimal conditions were found to be dispersion in MeOH with tip ultrasonication (see ESI† for details), and posterior 1 : 4 dilution with $CHCl_3$ for a final concentration of 0.3 mg mL^{-1}. DLS estimates the hydrodynamic diameter of the dispersed particles, which is usually somewhat larger than the actual particle diameter. Here the log-normal size distributions actually agree very well with sizes derived from SEM (Fig. 1 and Fig. S4, S5, ESI†), and the sizes are overall lower than twice the particle diameters, in agreement with well-dispersed particles. After spreading these dispersions on a water subphase in a Langmuir trough, compression leads to π–A isotherms with similar slopes and areas per mass of $Gd_xY_{1-x}OHCO_3$ particles for all particle compositions and sizes (Fig. S11, ESI†). Slight variations are ascribed to the large volumes required to form dense Langmuir films. A characteristic isotherm (Fig. 3(a)) shows a very gradual increase of the surface pressure starting from *ca.* 170 cm^2 mg^{-1} up to a plateau at *ca.* 38 mN m^{-1} in the range of 20–10 cm^2 mg^{-1}. Further compression induces an abrupt increase to reach 55 mN m^{-1} just before the collapse of the Langmuir film. Brewster Angle Microscopy images obtained during film formation indicate an almost full coverage of the water surface already at 5 mN m^{-1}. Similar images albeit with increasing intensities are obtained upon compression indicating densification but *a priori* no significant modifications of the film packing. LB films were thus initially transferred onto Si wafers at an intermediate pressure of 10 mN m^{-1}, but SEM observations showed only very poor substrate coverage (Fig. S12, ESI†), which could indicate that the packing is in fact not sufficiently compact at these pressures and/or the Langmuir film is not transferred efficiently. The former may explain the very gradual π–A isotherm. The plateau observed at *ca.* 38 mN m^{-1} could thus correspond to the film becoming truly compact only at these high pressures and small areas, very close to the collapse. Transfer was therefore done at 55 mN m^{-1}, resulting now in dense monolayers of $Gd_xY_{1-x}OHCO_3$ particles (Fig. 3(b) and Fig. S13, S14, ESI†). Compared with similar studies on particles of porous materials of similar sizes,[30] the much more gradual π–A isotherm and the relative difficulty in transferring dense LB films are probably in part due to the much higher density of the material.

Although we succeeded in transferring compact LB films homogeneously over large areas of Si wafers (Fig. S13, ESI†), the particles packing in these films and therefore the density of the film is affected by the presence of moderate particle size dispersion, which gives rise to packing defects. Under optimal conditions, a highly packed 2D layer of 222(31) nm particles covers *ca.* 73% of the Si substrate (Fig. 3(b) and Fig. S14, S15 (ESI†), the planar density for a perfect hexagonal arrangement of identical spherical particles is 90.7%), with free spaces arising between separated domains of sizes in the range 1–2 μm and on average 28–33 particles (see Fig. S16, ESI† for details). Within each domain, particles are ordered in hexagonal or square and hexagonal mixed arrangements (see examples highlighted in Fig. 3(b)). Local instances of the hexagonal packing expected for spherical particles are clearly observed, but due to the dispersion in particle diameter, some hexagonal arrangements are not perfect, and particles appear surrounded by six or seven neighbors (in the latter the central particle is highlighted in Fig. 3(b)), depending on the relative size particle/neighbor. Altogether, the coexistence of these arrangements is at the origin of the observed randomly oriented domains (Fig. S17, ESI†), impeding long-range ordering of the particles. Inspection and FFT analysis of small areas of the obtained LB films, however, shows that there exists short-range order when the particle sizes do not differ significantly (Fig. 3(b) right and Fig. S18, ESI†). Indeed, reciprocal points in the quasi-hexagonal arrangement are then observed with distances corresponding to the characteristic inter-particle space of the hexagonal arrangement (111 and 127 nm, theoretically 73% of particles size) and the inter-particle distances between large (242 nm) particles.

Transfer onto a chip with superconducting Lumped Element Resonators was then done under the same optimal conditions. Despite the complex structure of superconducting Nb lines with *ca.* 0.5 μm heights, the film covers homogeneously the whole chip surface and presents very similar characteristics to those obtained on flat Si (Fig. 3(c) and Fig. S19, ESI†). This is clearly seen by comparing structures that are parallel or perpendicular to the immersion direction of the chip during the vertical LB transfer. In both situations, the particles fully cover both the lower Si surface and the higher Nb surface until its edges (Fig. 3(c) right). This is important since the latter are the most sensitive areas of the superconducting lines, as the local magnetic field there is maximal.[10,13]

Chemical and magnetic characterization of deposited particles

Although the shape and size of the particles are clearly maintained once transferred to substrates, the absence of modification of the particles was further investigated by X-ray photo-electron spectroscopy on the optimized deposit of $Gd_{0.003}Y_{0.997}OHCO_3$ on Si (Fig. 4(a)). The survey spectrum is very similar to that of the starting powder material, showing the presence of the expected elements, in addition to Si from the substrate (Fig. S20, ESI†). In both cases, Gd peaks are not clearly detected, due to its low concentration. Nevertheless, high resolution Gd 3d spectra confirm the presence of Gd, with a $3d_{5/2}$ band at *ca.* 1187.6 eV, very similar in both the deposit and powder material, and in good agreement with reported values for Gd(III) metal–organic materials.[31] Note that observation of the Gd $3d_{3/2}$ band is impeded by the KLL Auger band of C. The O 1s peaks around 532 eV are also very similar. In the case of the bulk powder, it can be reproduced with three components, two main ones at respectively 531.3 and 532.0 eV

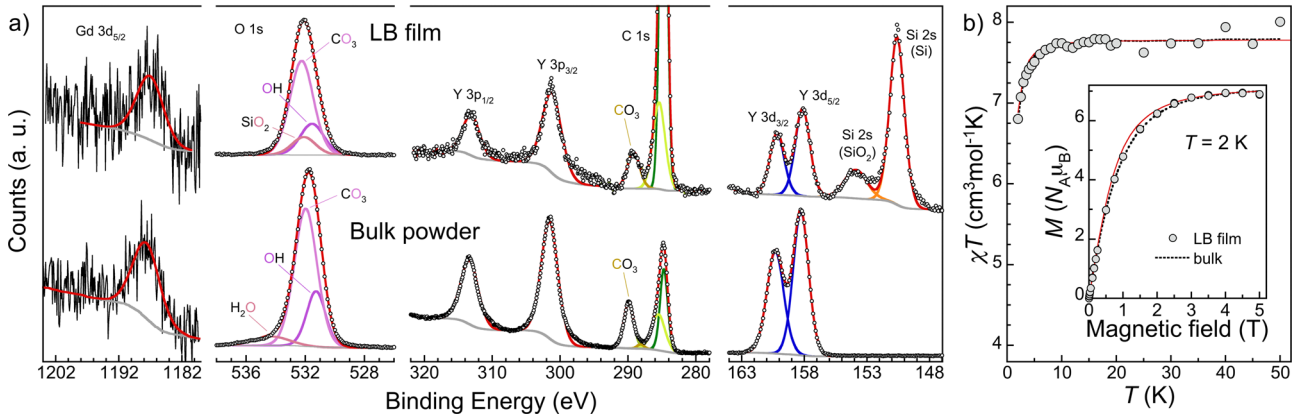

Fig. 4 (a) High resolution XPS spectra obtained for an optimized LB film of $Gd_{0.003}Y_{0.997}OHCO_3$ particles on Si (top) compared with those of the bulk original particles (bottom). Full lines represent the used Shirley or offset-Shirley background (grey), best fit components (various colours) and resulting envelope spectra (red). (b) χT *vs.* T plot and magnetization isotherm at 2 K (inset) for an optimized LB film of $Gd_{0.003}Y_{0.997}OHCO_3$ particles on Si. The solid red lines are respectively the curve calculated with the *curry* function of Easyspin[24] with the same parameters as those used to simulate the cw-EPR spectrum (see text) and the Brillouin function for $S = 7/2$ and $g = 2.02$. All data are scaled to pure $GdOHCO_3$. The dashed black lines depict the properties of the same particles in the bulk.

corresponding to the expected carbonate and hydroxyl oxygens,[32] and a smaller one at 534.3 eV likely due to water. The ratio of the two main components is *ca.* 1 : 3 in agreement with the hydroxycarbonate formulation. In the case of the deposit, the detection of Si from the substrate evident in the survey spectrum implies the presence of an oxide component corresponding to the native SiO_2 layer. The spectrum is nevertheless well reproduced with the oxide component at 532.1 eV (its area being fixed to agree with that of the Si 2s band) and two additional components in a 1 : 3 ratio at 531.5 and 532.2 eV, again in agreement with the expected carbonate and hydroxyl oxygens. The C 1s region shows a distinct peak at 289.3/289.2 eV respectively for the deposit/bulk powder, clearly corresponding to the carbonate C,[32] in addition to other components at lower binding energies corresponding to adventitious carbon, more prominent in the case of the LB deposit. In the same energy range, the Y $3p_{3/2}$ and $3p_{1/2}$ bands observed at 301.5/301.2 and 313.3/313.1 eV are again very similar in the deposit/bulk material. Eventually, the Y $3d_{5/2}$ and $3d_{3/2}$ peaks are found at 158.3/158.1 and 160.3/160.2 eV, respectively, for the deposit/bulk powder. Importantly, the FWHM of the Gd and Y bands are also similar and altogether the data point to the presence of only one type of Gd/Y environment. Eventually, the semi-quantitative ratios $Y/O_{carbonate}$ are in reasonable agreement with the expected 1/3 value, and similar in both the deposit/bulk powder, at 0.36/0.38. The Gd/Y ratio is also found to be similar for the deposit and bulk powder, at *ca.* 0.008, and in line with the level of dilution. The very small amount of Gd, however, implies that it should only be taken as qualitative, due to the intrinsic limitations of the XPS semi-quantitative analysis.

Clearly, the XPS observations support the chemical robustness of the pre-formed particles throughout the process of colloidal dispersion and LB transfer. In addition to these, the magnetic properties of the LB film were determined and compared to those of the starting powder material and the model derived from EPR spectroscopy. After correction for the diamagnetic contribution of the Si substrate, determined separately, both the M *vs.* H data at 2 K and the χT *vs.* T plot are virtually identical to those of the bulk material (see Fig. 4(b)), once scaled by a factor corresponding to *ca.* 1.50×10^{-10} mole of Gd(III). Considering the size of the piece of Si measured, 0.4×0.6 cm^2, and the fact that it is covered on both sides by the particle LB film, this yields a surface density of 1.88×10^{14} Gd cm^{-2}, in line with the value of 1.42×10^{14} calculated considering the nominal composition $Gd_{0.003}Y_{0.997}OHCO_3$ and the particle density and size derived from analysis of SEM images (see above). The slightly higher density derived through magnetic measurements may be ascribed to the presence of some additional particles stacked over the first monolayer, as indeed observed.

Controlled localization through Dip-Pen Nanolithography and AFM stamping

The ability to dispose isolated particles in a controlled manner at specific positions of a device was studied using DPN. For this, a sufficiently stable and concentrated colloidal dispersion in a poorly-volatile and relatively viscous solvent is required as ink. Among a range of solvents and MeOH–glycerol mixtures tested, DMF was found to be optimal, allowing 0.5 mg mL^{-1} dispersions without the necessity of any additive and with good polydispersity, as derived through DLS measurements (Fig. 5(a)). Initial experiments showed that the size of the particles does not allow their transport to be controlled by diffusion, as normally done with DPN for molecular materials.[14] Instead, transference was achievable as a liquid ink composed of the particles suspended in the ink solvent. DPN deposition on Si was thus done by first charging the DPN cantilever by immersion in a micro-droplet of the DMF dispersion on a Si wafer. After four successive bleedings of the

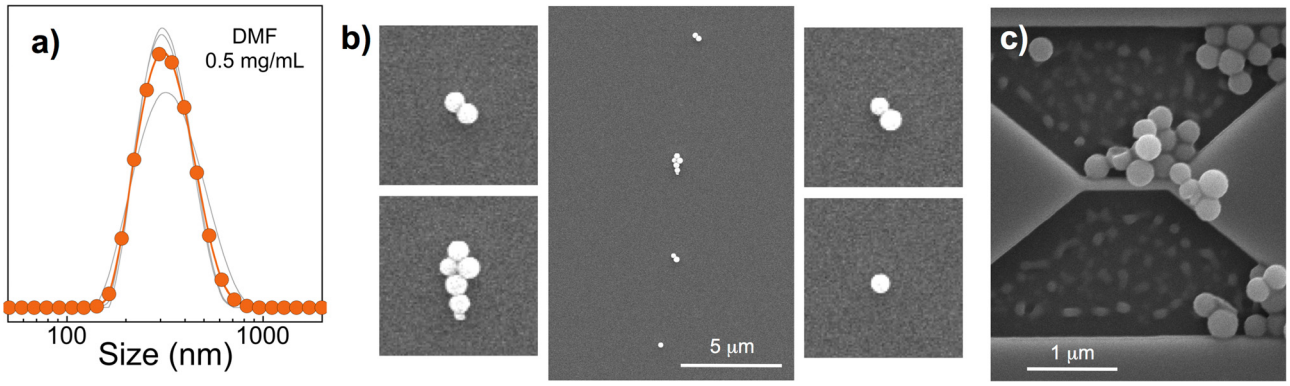

Fig. 5 (a) DLS hydrodynamic size distribution obtained for a DMF dispersion of $Gd_{0.003}Y_{0.997}OHCO_3$ particles. The orange dot + line is the average of three consecutive measurements shown as grey lines. (b) SEM image of particles deposited on Si through DPN line writing at 0.2 mm s^{-1} using a 0.5 mg mL^{-1} DMF dispersion as ink, after initial cantilever bleeding. (c) SEM image of a typical deposit made through AFM tip stamping in the vicinity of a nanoconstriction in a Nb superconducting line, using the same ink.

cantilever, line-writing at 0.2 mm s^{-1} over a 30 μm distance allows to deposit well isolated groups of 1 to 5 particles (Fig. 5(b)). Note that the cantilever bleeding steps already leave relatively isolated groups of few particles (Fig. S21, ESI†). To the best of our knowledge, these results represent the first report of deposition of particles of sizes above 100 nm through DPN.[14]

Alternatively, we also studied the possibility to use a standard AFM, soaking its cantilever in a drop of the same DMF dispersion, and stamping it under a variety of conditions on Nb nanoconstrictions. When stamping is done maintaining the tip-surface interaction weak, *i.e.* through the DMF, no particles are deposited (Fig. S22, ESI†), probably due to a poor diffusion within the ink nano-droplet. On the contrary, a strong tip-surface contact interaction leaves groups of particles in the vicinity of nanoconstrictions, provided the cantilever charge is not excessive (Fig. 5(c) and Fig. S21, ESI†). The necessity of a strong contact interaction, however, limits the spatial resolution to the width of the cantilever. Also, the relatively large volume of ink left on the substrate likely results in the aggregation of groups of particles upon slow evaporation of the DMF solvent, as observed. Clearly, without the optimized conditions of a dedicated DPN set-up, the control of localization and particle isolation obtained is not sufficient. We, however, are confident that deposits with 1–5 particles should be obtained on the Nb surface of nanoconstrictions using similar DPN conditions as those used for Si.

Conclusions

Spherical particles of amorphous Y(III) hydroxycarbonate can be obtained with various degrees of doping with Gd(III) ions in the range of 0.2 to 10% and diameters between 190 and 350 nm, thus providing a control over the number of spins per particle down to the tens of thousands. The Gd(III) ions in these particles are well isolated magnetically, and present weak anisotropy, with an estimated zero-field splitting term D of 1.12 GHz, quantum coherence, with reasonable phase-memory times T_M up to 0.7 μs, and relatively long – for a Gd(III) species – spin–lattice relaxation times T_1, up to 30 μs at 6 K, altogether making them viable spin qubits. The particle robustness allows obtaining stable colloidal dispersions in organic solvents, which in turn opens the use of Langmuir–Blodgett and Dip-Pen Nanolithography techniques. With the former, densely-packed particle monolayers are successfully transferred to either Si wafer or chips with Nb superconducting structures. Through the latter, isolated groups of few – including single – particles can be deposited with a fine control of their localization. The reported strategy therefore provides the means to integrate ensembles of an adjustable number of spin qubits onto superconducting devices, including with nanoscopic control. These results are relevant for the development of a viable hybrid quantum computing architecture.

Conflicts of interest

There are no conflicts of interest to declare.

Acknowledgements

This research was supported by the European Union Horizon 2020 research and innovation program through FET-OPEN grant FATMOLS-No 862893, the Spanish MCIN/AEI/10.13039/501100011033 and ERDF "A way of making Europe" (projects PID2019-105881RB-I00 and PID2020-1183294RB-I00), the Aragón government (PLATON E31_20R and E31_23R, doctoral grant to IT), and the CSIC Research Platform PTI-001 QUTEP. We are grateful to Drs I. Gimeno and F. Luis (INMA) and A. Gómez (CAB) for providing test chips with Nb superconducting LERs and nanoconstrictions, as well as to Dr G. Antorena for XPS measurements done through the Laboratorio de Microscopías Avanzadas (LMA).

References

1 (*a*) J. M. Martinis, *et al.*, *Nature*, 2019, **574**, 505–510; (*b*) E. Pednault, J. A. Gunnels, G. Nannicini, L. Horesh and R. Wisnieff, arXiv, 1910.09534v2.

2 the error rate per gate for 2-qubit gates is still at 0.1% or worse, see J. Preskill, *Quantum*, 2018, **2**, 79 or arXiv:1801.00862v3.

3 (*a*) IBM quantum roadmap involves reaching 10–100 K qubits, see **https://www.ibm.com/quantum/roadmap**, consulted on 31/05/2023; (*b*) A. G. Fowler, M. Mariantoni, J. M. Martinis and A. N. Cleland, *Phys. Rev. A: At., Mol., Opt. Phys.*, 2012, **86**, 032324; (*c*) Google Quantum AI, *Nature*, 2023, **614**, 676–681.

4 T. D. Ladd, F. Jelezko, R. Laflamme, Y. Nakamura, C. Monroe and J. L. O'Brien, *Nature*, 2010, **464**, 45–53.

5 (*a*) A. Ardavan, O. Rival, J. J. L. Morton, S. J. Blundell, A. M. Tyryshkin, G. A. Timco and R. E. P. Winpenny, *Phys. Rev. Lett.*, 2007, **98**, 057201; (*b*) A. Gaita-Ariño, F. Luis, S. Hill and E. Coronado, *Nat. Chem.*, 2019, **11**, 301–309; (*c*) G. Aromí and O. Roubeau, in *Handbook on the Physics and Chemistry of Rare Earths*, ed. J. C. G. Bunzli and V. K. Pecharsky, 2019, vol. 56, pp. 1–54; (*d*) E. Moreno-Pineda, D. O. T. A. Martins and F. Tuna, *Electron Paramagn. Reson.*, 2021, **27**, 146–187.

6 (*a*) K. Bader, D. Dengler, S. Lenz, B. Endeward, S.-D. Jiang, P. Neugebauer and J. van Slageren, *Nat. Commun.*, 2014, **5**, 5304; (*b*) J. Zadrozny, J. Niklas, O. G. Poluetkov and D. E. Freedman, *Cent. Sci.*, 2015, **1**, 488.

7 G. Aromí, D. Aguilà, P. Gamez, F. Luis and O. Roubeau, *Chem. Soc. Rev.*, 2012, **41**, 537–546; D. Aguilà, O. Roubeau and G. Aromí, *Dalton Trans.*, 2021, **50**, 12045–12057.

8 (*a*) E. Macaluso, M. Rubín, D. Aguilà, A. Chiesa, L. A. Barrios, J. I. Martínez, P. J. Alonso, O. Roubeau, F. Luis, G. Aromí and S. Carretta, *Chem. Sci.*, 2020, **11**, 10337; (*b*) A. Chiesa, F. Petiziol, M. Chizzino, P. Santini and S. Carretta, *J. Phys. Chem. Lett.*, 2022, **28**, 6468.

9 (*a*) S. Thiele, F. Balestro, R. Ballou, S. Klyatskaya, M. Ruben and W. Wernsdorfer, *Science*, 2014, **344**, 1135–1138; (*b*) C. Godfrin, A. Ferhat, R. Ballou, S. Klyatskaya, M. Ruben, W. Wernsdorfer and F. Balestro, *Phys. Rev. Lett.*, 2017, **119**, 187702.

10 (*a*) M. D. Jenkins, D. Zueco, O. Roubeau, G. Aromí, J. Majer and F. Luis, *Dalton Trans.*, 2016, **45**, 16682; (*b*) S. Carretta, D. Zueco, A. Chiesa, A. Gómez-Léon and F. Luis, *Appl. Phys. Lett.*, 2021, **118**, 240501; (*c*) A. Chiesa, S. Roca, S. Chicco, M. C. de Ory, A. Gómez-León, A. Gomez, D. Zueco, F. Luis and S. Carretta, *Phys. Rev. Appl.*, 2023, **19**, 064060.

11 (*a*) I. Gimeno, A. Urtizberea, J. Román-Roche, D. Zueco, A. Camón, P. J. Alonso, O. Roubeau and F. Luis, *Chem. Sci.*, 2021, **12**, 5621–5630; (*b*) V. Rollano, M. C. De Ory, C. D. Buch, M. Rubín-Osanz, D. Zueco, C. Sánchez-Azqueta, A. Chiesa, D. Granados, S. Carretta, A. Gomez, S. Piligkos and F. Luis, *Commun. Phys.*, 2022, **5**, 246; (*c*) C. Bonizzoni, A. Ghirri, K. Bader, J. van Slageren, M. Perfetti, L. Sorace, Y. Lan, O. Fuhr, M. Ruben and M. Affronte, *Dalton Trans.*, 2016, **45**, 16496; (*d*) C. Bonizzoni, A. Ghirri, M. Atzori, L. Sorace, R. Sessoli and M. Affronte, *Sci. Rep.*, 2017, **7**, 13086; (*e*) C. Bonizzoni, A. Ghirri, F. Santanni, M. Atzori, L. Sorace, R. Sessoli and M. Affronte, *npj Quantum Inf.*, 2020, **6**, 68.

12 (*a*) K. Yang, W. Paul, S.-H. Phark, P. Willke, Y. Bae, T. Choi, T. Esat, A. Ardavan, A. J. Heinrich and C. P. Lutz, *Science*, 2019, 509–512; (*b*) S.-H. Phark, Y. Chen, H. T. Bui, Y. Wang, M. Haze, J. Kim, Y. Bae, A. J. Heinrich and C. Wolf, *ACS Nano*, 2023, **17**, 14144–14151; (*c*) C. Godfrin, A. Ferhat, R. Ballou, S. Klyatskaya, M. Ruben, W. Wernsdorfer and F. Balestro, *Phys. Rev. Lett.*, 2017, **119**, 187702; (*d*) H. Biard, E. Moreno-Pineda, M. Ruben, E. Bonet, W. Wernsdorfer and F. Balestro, *Nat. Commun.*, 2021, **12**, 4443 and references therein.

13 M. D. Jenkins, U. Naether, M. Ciria, J. Sesé, J. Atkinson, C. Sánchez-Azqueta, E. Del Barco, J. Majer, D. Zueco and F. Luis, *Appl. Phys. Lett.*, 2014, **105**, 162601.

14 G. Liu, S. Hurst Petrosko, Z. Zheng and C. A. Mirkin, *Chem. Rev.*, 2020, **120**, 6009.

15 I. Gimeno, W. Kersten, M. C. Pallarés, P. Hermosilla, M. J. Martínez-Pérez, M. D. Jenkins, A. Angerer, C. Sánchez-Azqueta, D. Zueco, J. Majer, A. Lostao and F. Luis, *ACS Nano*, 2020, **14**, 8707.

16 (*a*) G. Serrano, L. Poggini, M. Briganti, A. L. Sorrentino, G. Cucinotta, L. Malavolti, B. Cortigiani, E. Otero, P. Sainctavit, S. Loth, F. Parenti, A.-L. Barra, A. Vindigni, A. Cornia, F. Totti, M. Mannini and R. Sessoli, *Nat. Mater.*, 2020, **19**, 546–551; (*b*) A. L. Sorrentino, I. Cimatti, G. Serrano, L. Poggini, B. Cortigiani, L. Malavolti, E. Otero, P. Sainctavit, M. Mannini, R. Sessoli and A. Caneschi, *J. Mater. Chem. C*, 2021, **9**, 15011; (*c*) M. Briganti, G. Serrano, L. Poggina, A. L. Sorrentino, B. Cortigiani, L. C. de Camargo, J. F. Soares, A. Motta, A. Caneschi, M. Mannini, F. Totti and R. Sessoli, *Nano Lett.*, 2022, **22**, 8626–8632.

17 L. Malavolti, M. Briganti, M. Hänze, G. Serrano, I. Cimatti, G. McMurtrie, E. Otero, P. Ohresser, F. Totti, M. Mannini, R. Sessoli and S. Loth, *Nano Lett.*, 2018, **18**, 7955–7961.

18 (*a*) A. Urtizberea, E. Natividad, P. J. Alonso, M. A. Andrés, I. Gascón, M. Goldmann and O. Roubeau, *Adv. Funct. Mater.*, 2018, **28**, 1801695; (*b*) A. Urtizberea, E. Natividad, P. J. Alonso, L. Pérez-Martínez, M. A. Andrés, I. Gascón, I. Gimeno, F. Luis and O. Roubeau, *Mater. Horiz.*, 2020, **7**, 885–897.

19 (*a*) M. J. Martínez-Pérez, S. Cardona-Serra, C. Schlegel, F. Moro, P. J. Alonso, H. Prima-García, J. M. Clemente-Juan, M. Evangelisti, A. Gaita-Ariño, J. Sesé, J. van Slageren, E. Coronado and F. Luis, *Phys. Rev. Lett.*, 2012, **108**, 247213; (*b*) M. D. Jenkins, Y. Duan, B. Diosdado, J. J. García-Ripoll, A. Gaita-Ariño, C. Gimenez-Saiz, P. J. Alonso, E. Coronado and F. Luis, *Phys. Rev. B*, 2017, **95**, 8; (*c*) F. Luis, P. J. Alonso, O. Roubeau, V. Velasco, D. Zueco, D. Aguilà, J. I. Martínez, L. A. Barrios and G. Aromí, *Commun. Chem.*, 2020, **3**, 176; (*d*) Y.-H. Fang, Z. Liu, Y.-X. Wang, S. Zhou, S.-D. Jiang and S. Gao, *Inorg. Chem. Front.*, 2020, **7**, 3875–3881.

20 (*a*) E. Matijevic and W. P. Hsu, *J. Colloid Interface Sci.*, 1987, **118**, 506–523; (*b*) B. Aiken, W. P. Hsu and E. Matijevic, *J. Am. Ceram. Soc.*, 1988, **71**, 845–853; (*c*) D. Sordelet and M. Akinc, *J. Colloid Interface Sci.*, 1988, **122**, 47–59.

21 (*a*) K. Nakamoto, *Infrared and Raman spectra of Inorganic and Coordination Compounds*, John Wiley & Sons, 6th edn, 2009; (*b*) K. Makamoto, J. Fujita, S. Tanaka and M. Kobayashi,

J. Am. Chem. Soc., 1957, **57**, 495; (*c*) P. C. Healy and A. H. White, *Spectrochim. Acta, Part A*, 1973, **29**, 1191.

22 (*a*) Y.-C. Chen, L. Qin, Z.-S. Meng, D.-F. Yang, C. Wu, Z. Fu, Y.-Z. Zheng, J.-L. Liu, R. Tarasenko, M. Orendác, J. Prokleska, V. Sechovsky and M.-L. Tong, *J. Mater. Chem. A*, 2014, **2**, 9851; (*b*) R. J. C. Dixey and P. J. Saines, *Inorg. Chem.*, 2018, **57**, 12543; (*c*) M. Hämmer and A. Höppe, *Z. Naturforsch. B*, 2019, **74**, 59.

23 I. Tejedor, E. Natividad, I. Gascón and O. Roubeau, unpublished results, see also ref. 22a and b.

24 S. Stoll and A. Schweiger, *J. Magn. Reson.*, 2006, **178**, 42–55.

25 D = 1.20 GHz and $|E|$ = 86 MHz at 295 K for a powder sample, see ref. 19b.

26 the Debye temperature of crystalline $GdOHCO_3$ has been reported to be 313 K, see ref. 22*a*.

27 this is for example the case at the clock transitions in HoW_{30}, see M. Shiddiq, D. Komijani, Y. Duan, A. Gaita-Ariño, E. Coronado and S. Hill, *Nature*, 2016, **531**, 348.

28 S. Cardona-Serra, L. Escalera-Moreno, J. J. Baldoví, A. Gaita-Ariño, J. M. Clemente-Juan and E. Coronado, *J. Comput. Chem.*, 2016, **37**, 1238.

29 Simulation of the 500 mT data. Note that the Raman exponent has been fixed at 9 following the original work of Orbach for Kramers ions, see R. Orbach, *Proc. R. Soc. London, Ser. A*, 1961, **264**, 458.

30 (*a*) J. Benito, S. Sorribas, I. Lucas, J. Coronas and I. Gascón, *ACS Appl. Mater. Interfaces*, 2016, **8**, 16486; (*b*) M. A. Andrés, P. Fontaine, M. Goldmann, C. Serre, O. Roubeau and I. Gascón, *J. Colloid Interface Sci.*, 2021, **590**, 72.

31 (*a*) J. I. Urgel, B. Cirera, Y. Wang, W. Auwärter, R. Otero, J. M. Gallego, M. Alcamí, S. Klyatskaya, M. Ruben, F. Martín, R. Miranda, D. Ecija and J. V. Barth, *Small*, 2015, **11**, 6358–6364; (*b*) O. Roubeau, E. Natividad, M. Evangelisti, G. Lorusso and E. Palacios, *Mater. Horiz.*, 2017, **4**, 464–476; (*c*) G. Lorusso, E. Natividad, M. Evangelisti and O. Roubeau, *Mater. Horiz.*, 2019, **6**, 144–154; (*d*) H. Brunckova, E. Mudra, L. Rocha, E. Nassar, W. Nascimento, H. Kolev, A. Kovalcikova, Z. Molcanova, M. Podobova and L. Medvecky, *Appl. Surf. Sci.*, 2021, **542**, 148731.

32 J. Yang, H. Cheng and R. L. Frost, *Spectrochim. Acta, Part A*, 2011, **78**, 420–428.

